INTERNATIONAL JOURNAL FOR NUMERICAL METHODS IN FLUIDS
Int. J. Numer. Meth. Fluids **26**: 1003–1022 (1998)

A THREE-DIMENSIONAL SIMULATION OF A STEADY APPROACH FLOW PAST A CIRCULAR CYLINDER AT LOW REYNOLDS NUMBER

JIANFENG ZHANG AND CHARLES DALTON*

Department of Mechanical Engineering, University of Houston, Houston, TX 77204-4792, USA

SUMMARY

The three-dimensional (3D) unsteady viscous wake of a circular cylinder exposed to a steady approach flow is calculated using a fractional-step finite-difference/spectral-element method. The calculated flow fields at Reynolds numbers of 100 (2D) and 200 (3D) are examined in detail. The flow field at $Re = 100$ is 2D as expected, while the flow field at $Re = 200$ has distinct 3D features, with spanwise wavelengths of about 3.75 cylinder diameters. The calculated results produce drag and lift coefficients and Strouhal numbers that agree extremely well with the experimental values. These 3D values at $Re = 200$ are in better agreement with experimental values than the results of a 2D calculation at $Re = 200$, which is expected. © 1998 John Wiley & Sons, Ltd.

KEY WORDS: steady approach flow; low Reynolds numbers; 3D simulation

1. INTRODUCTION

The flow in the wake of a circular cylinder is three-dimensional (3D), even before it becomes turbulent. The present study concerns the combined finite difference/spectral method calculation of the steady approach flow past a fixed circular cylinder at Reynolds numbers large enough for the wake to be three-dimensional, but not turbulent. The onset of the 3D wake will be discussed and it will be shown that the proper representation of the wake has a noticeable effect on the Strouhal number and the drag and lift coefficients. Specifically, the flow will be represented in terms of the primitive-variables form of the time-dependent Navier–Stokes equations for an incompressible fluid. A fractional-step method, which is a combination of the methods of Karniadakis *et al.* [1] and Kim and Moin [2], is used to advance the solution in time.

For a circular cylinder in a steady approach flow, the 2D vortex structures are unstable to 3D disturbances at a Reynolds number of about 170. A synopsis of the steady approach flow situation follows. When the Reynolds number, $Re = UD/v$, where U, D, and v are, respectively, the freestream velocity, diameter of the cylinder, and kinematic viscosity of the fluid, is smaller than 40, the flow is steady with two symmetrical vortices attached to the downstream side of the cylinder. When the Reynolds number is slightly larger, $Re < 60$, the trailing vortex sheet becomes unstable and develops an unsteady wavy pattern. Vortex shedding occurs for $60 < Re < 170$; the attached vortices become asymmetric and are shed alternately at a

* Correspondence to: Department of Mechanical Engineering, University of Houston, Houston, TX 77204-4792, USA.

CCC 0271–2091/98/091003–23$17.50

Received 26 April 1996
Revised 9 December 1996

well-defined frequency, the Strouhal frequency (S), to form the Karman vortex sheet behind the cylinder. When Re is greater than 170, the vortex structures are unstable to 3D perturbations. Past research has found several different vortex shedding modes in the transitional regime $170 < Re < 400$. Bloor [3] found that transition to turbulence occurs in the region $200 < Re < 400$. The wake becomes fully turbulent when Re is higher than 400 according to Bloor's measurements.

Roshko [4] was one of the first to make extensive measurements in the wake. Roshko observed that the vortex street is stable for Re under 150 and irregular when Re is higher than 300.

Hama [5] studied the development of 3D flows. Hama's flow visualization showed that three-dimensionality is not present for $Re < 150$. It appears intermittently for $150 < Re < 200$ and becomes regular for $200 < Re < 300$. Hama also observed that the spanwise wavelength decreases by a factor of about 3 from $Re < 200$ to Re of about 300. In Gerrard [6], finger-like structures are observed in flow visualizations and correspond to the spanwise waviness of the shed vortices. Gerrard found that these structures appear almost randomly along the primary vortices, but they repeat at the same location, cycle after cycle of vortex shedding.

Williamson [7] found that two discontinuities exist in the S–Re relationship in this transitional regime. The first discontinuity occurs at Re between 170 and 180, and corresponds to the secondary flow that takes the form of vortex loops. This discontinuity shifts vortex shedding toward the lower frequency. Williamson's flow visualization pictures show that the spanwise wavelength is slightly smaller than three diameters. At the second discontinuity, which occurs at Re between 230 and 260, finer scales develop in the streamwise vortex structure, and vortex shedding is shifted to a higher frequency. The spanwise wavelength after this discontinuity is about one diameter. Recently, Noack and Eckelmann [8] did a global 3D stability analysis using a low-dimensional Galerkin method. They found that the periodic solution (parallel vortex shedding) is unstable to spanwise perturbations for $Re > 170$ and is most unstable to a perturbation with a spanwise wavelength of 1.8 diameters. For Re between 54 and 170, the periodic solution is neutrally stable, which explains the difficulty in experiments to achieve parallel vortex shedding. The results by Noack and Eckelmann do not show the second discontinuity which was observed also by König *et al.* [9]. They attributed the discrepancy to be possibly because of the realization of end conditions. The end conditions are important for the Reynolds number between the two discontinuities even at large aspect ratios, and these conditions are not full realized in numerical simulations. The numerically assigned periodicity may also introduce or prohibit perturbations of certain wavelengths. Mansy *et al.* [10] measured 3D structures in the wake and found the spanwise wavelength at 6 diameters downstream from the center of the cylinder is 3.2 diameters at Re of about 200. The wavelength undergoes a discontinuous change at Re of about 300 to 1.1 diameters. The wavelength-to-diameter ratio approximately follows a relationship of $20/Re^{0.5}$. They also observed the high sensitivity of wavelength to streamwise direction location in the near wake. The wavelength is most sensitive within 6 diameters from the cylinder and increases with streamwise location to reach an asymptotic value at 15 diameters from the cylinder. The 3D structures observed by Mansy *et al.* are regular for Re above 180–200 and intermittent for Re between 160 and 180. Bays-Muchmore and Ahmed [11] used a flow-visualization method to study the streamwise vortices in the wake, with Re from 330 to 21 000. Their observations are consistent with those of Mansy *et al.* The pairs of counter-rotating vortices have spanwise spacings of about one diameter. Bays-Muchmore and Ahmed observed that these vortices distort the Karman vortices significantly, but 'only on their upstream sides'.

Three-dimensionality in the wake of a circular cylinder takes on several different forms. Beside the forms described above, vortex dislocation is another important form. For some flow conditions, nonuniform vortex shedding occurs and vortices reconnect between cells of vortex shedding in the wake. In the region of dislocation, the variation in vorticity is more irregular than at other places. The stronger tilting and stretching of vortices in these regions can promote transition to turbulence. Vortex dislocation has been studied by many researchers, among which are Williamson [12], Lewis and Gharib [13], Williamson [14], and Yang *et al.* [15]. The end effects on the modes of vortex shedding, including parallel vortex shedding, oblique vortex shedding, and vortex dislocations, are clearly shown by Hammache and Gharib [16]. They found that oblique vortex shedding can be avoided if special care is given to the end conditions. Enforcement of parallel shedding by reducing end effects also delays the transition to turbulence through reduction of the number of vortex dislocations.

Numerical simulations of 2D vortex shedding have been studied by many people using quite different numerical methods, e.g., [17–22]. However, as noted by Karniadakis and Triantafyllou [23], three-dimensionality is 'an unavoidable state of even nominally 2D wakes, once a certain critical Reynolds number is exceeded'. Moreover, transition is inherently 3D, as shown in the experiments of Hammache and Gharib [16]. Therefore, 3D simulations are necessary to understand the dynamics of the flow with Re greater than the critical Reynolds number for 3D instability. Karniadakis and Triantafyllou [23] used a 3D direct numerical simulation based on a combined spectral element/Fourier spectral method to study flows with Re between 175 and 500. The streamwise structures shown have a wavelength of 0.8 diameters at $Re = 225$ and $Re = 300$, which is in reasonable agreement with the observed wavelength of 1.1 diameters for $Re = 300$ [10]. For Re at 300, they found the variation of velocity in the wake oscillates at double the period it had at $Re = 225$. This period-doubling phenomenon was attributed to the two modes of vortex motion when three-dimensionality is present. This behavior continues (more and more subharmonics appear) when Re increases, and is the route for transition, according to Karniadakis and Triantafyllou. To assess the influence of the size of the spanwise computational domain, they used 1.57 and 3.14 diameters and found no essential difference in the period doubling phenomena between the results from the two different domain lengths, but they noted that the strength of secondary flow is much stronger with the larger computational domain. Another numerical study of 3D flows is by Hansen *et al.* [24], who used the velocity–vorticity formulation of the Navier–Stokes equation and simulated the flow around an infinite cylinder at $Re = 200$. Their results show 3D structures with a spanwise wavelength of about three diameters.

In this paper, the numerical solution of a steady approach flow past a circular cylinder at two values of Reynolds number ($Re = 100$, 200) is considered. Both Reynolds numbers are known to produce purely viscous flow with the wake, 2D at $Re = 100$ and 3D at $Re = 200$. A combined finite-difference/spectral method solution technique will be used with time advanced using a fractional-step method.

2. ANALYSIS

2.1. Governing equations

To describe the viscous transition from a 2D to a 3D wake in a steady approach flow past a fixed circular cylinder, the nondimensional versions of the continuity equation and the Navier–Stokes equation for an incompressible fluid are used,

$$\nabla \cdot \mathbf{v} = 0 \tag{1}$$

and

$$\frac{\partial \mathbf{v}}{\partial \tau} + (\nabla \times \mathbf{v}) \times \mathbf{v} = -\nabla \Phi + \frac{2}{Re} \nabla^2 \mathbf{v}, \tag{2}$$

where $\mathbf{v}$ is the nondimensional velocity vector, τ is the nondimensional time, Φ is the nondimensional pressure (including the kinetic energy) and Re is the Reynolds number defined earlier. In defining these nondimensional terms, the velocity scale is the approach velocity U, the length scale is the cylinder radius R, and the time scale is R/U. The pressure term is

$$\Phi = (p/\rho U^2) + (\mathbf{v} \cdot \mathbf{v}/2U^2),$$

where p is the dimensional pressure and ρ is the constant fluid density. In the actual computational scheme, the polar cylindrical form of Equations (1) and (2) are used.

The initial conditions for this problem are

$$u(r, \theta, z, 0) = \left(1 - \frac{1}{r^2}\right) \cos \theta, \tag{3}$$

$$v(r, \theta, z, 0) = -\left(1 + \frac{1}{r^2}\right) \sin \theta, \tag{4}$$

and

$$w(r, \theta, z, 0) = 0, \tag{5}$$

where U, the freestream velocity, has been set as unity and the dimensionless velocity components are u, v, and w in the r-, θ-, z-directions, respectively.

The boundary conditions are

$$u(1, \theta, z, \tau) = v(1, \theta, z, \tau) = w(1, \theta, z, \tau) = 0 \text{ on the cylinder.} \tag{6}$$

The inflow boundary condition is the uniform velocity at all inflow points. Special treatment of boundary conditions is necessary at the outer boundary ($r \to \infty$). For steady approach flows, a boundary condition is required that does not interfere with the passage of vortices or adversely influences the flow in the inner field. The outflow boundary conditions will be specified after the numerical representation is discussed.

In the circumferential direction, the natural periodic boundary condition applies,

$$f(r, \theta + 2\pi, z, \tau) = f(r, \theta, z, \tau), \tag{7}$$

where the functional $f(\,)$ refers to all three velocity components, u, v, and w.

The boundary conditions in the axial directions are not as straightforward as in the other two directions. Periodic conditions will be used in this direction also,

$$f(r, \theta, z + Z, \tau) = f(r, \theta, z, \tau), \tag{8}$$

where $f(\,)$ again refers to all three velocity components and Z is the imposed spanwise wavelength or its multiple. However, the natural wavelength changes with flow conditions and is unknown, so some judgements are necessary in determining the wavelength.

3. THE NUMERICAL REPRESENTATION

A mixed finite-difference and Fourier spectral representation of the physical problem in space is used. There are two dimensions in the physical model that have periodic boundary conditions. So, use of the Fourier spectral approximation in these dimensions brings significantly reduced computational cost to obtain 3D solutions because of the accuracy of the Fourier spectral methods.

The finite-difference representation is chosen for the radial direction because of its simplicity in implementation compared with the Chebyshev spectral approximation, which would be used if a spectral approximation were chosen in this direction with nonperiodic boundary conditions.

3.1. Fractional step method

A second-order accurate fractional-step method is used to discretize the governing equations in time. As mentioned earlier, this fractional-step method is a combination of the ideas of Karniadakis *et al.* [1] and Kim and Moin [2]. In this approach, an intermediate velocity, $\hat{\mathbf{v}}$, is first obtained by omitting pressure and using the second-order Adams–Bashforth scheme on the convective terms and the Crank–Nicolson scheme on the viscous terms. This intermediate velocity is corrected from a pressure Poisson equation to satisfy the continuity equation. Finally, the boundary conditions on velocity are applied to get the velocity at the next time step.

The intermediate velocity, $\hat{\mathbf{v}}$, is obtained from

$$\frac{\hat{\mathbf{v}}-\mathbf{v}^n}{\Delta\tau} = -\frac{1}{2}(3\mathbf{N}^n-\mathbf{N}^{n-1})+\frac{1}{2}\mathbf{L}^n, \tag{9}$$

where the superscripts refer to the time step, $\mathbf{N}$ represents the convective terms in (1), and $\mathbf{L}$ represents the viscous terms. The intermediate velocity is corrected by pressure to obtain a second intermediate velocity, $\tilde{\mathbf{v}}$, from

$$\frac{\tilde{\mathbf{v}}-\hat{\mathbf{v}}}{\Delta\tau} = -\nabla\Phi^{n+1/2}. \tag{10}$$

Finally, the velocity at time step $n+1$ is obtained by

$$\frac{\mathbf{v}^{n+1}-\tilde{\mathbf{v}}}{\Delta\tau} = \frac{1}{2}\mathbf{L}^{n+1}. \tag{11}$$

In Equation (10), the pressure head, Φ, is unknown. Since the intent is to satisfy the continuity equation for time step $n+1$, the divergence of Equation (11) is taken and set

$$Q^{n+1} = \nabla\cdot\mathbf{v}^{n+1} = 0, \tag{12}$$

and the following is obtained,

$$\tilde{Q} = \nabla\cdot\tilde{\mathbf{v}} = 0. \tag{13}$$

Then the divergence of Equation (10) is taken and Equation (13) is applied to get

$$\nabla^2\Phi^{n+1/2} = \frac{\nabla\cdot\hat{\mathbf{v}}}{\Delta\tau}. \tag{14}$$

After $\Phi^{n+1/2}$ is found from Equation (14) with appropriate boundary conditions (see Equations (16) and (17)), $\tilde{\mathbf{v}}$ and $\mathbf{v}^{n+1}$ can be calculated from Equations (10) and (11), respectively. No boundary conditions are necessary for either of the two intermediate velocities.

Although the divergence-free condition of the velocity is used at the next time step, Equation (12), to obtain the equation for pressure and the second intermediate velocity, a zero divergence of $\mathbf{v}^{n+1}$ is not automatically achieved because the continuity equation and the momentum equations have been uncoupled. Taking the divergence of Equation (11) and taking $\tilde{\mathbf{v}}$ to be divergence-free, the equation that is satisfied by the divergence of $\mathbf{v}^{n+1}$ is

$$\frac{Q^{n+1}}{\Delta\tau} = \frac{1}{Re}\nabla^2 Q^{n+1}. \tag{15}$$

This equation shows that the divergence of $\mathbf{v}^{n+1}$ satisfies a numerical boundary layer equation [1]. The divergence (Q^{n+1}) is zero only if it is zero on the boundary. For no-slip boundaries, it is difficult to control the divergence in the computational field. If not, the divergence will decrease with the normal distance from the boundary proportional to $O((\Delta\tau/Re)^{-1/2})$. The divergence in this numerical boundary can be $O(\Delta\tau)$, whereas the divergence in other parts of the flow field is $O(\Delta\tau^2)$. This could lead to large divergence or inaccurate solutions for some problems, especially if the solution for pressure needs to be accurate near solid walls, such as when fluid forces are of interest.

To control this time-splitting error, the consistent scheme developed by Karniadakis *et al.* [1] is used on the boundary condition for pressure on solid boundaries that have no velocity, i.e.,

$$\frac{\partial\Phi}{\partial n} = -\frac{2}{Re}\,\mathbf{n}\cdot\nabla\times(\nabla\times\mathbf{v}), \tag{16}$$

where n refers to the direction normal to the wall, and $\mathbf{n}$ is the unit normal vector. Karniadakis *et al.* [1] and related work showed that this 'rotational' boundary condition is superior to the traditional boundary condition,

$$\frac{\partial\Phi}{\partial n} = \frac{2}{Re}\,\mathbf{n}\cdot\nabla^2\mathbf{v}, \tag{17}$$

in that it eliminates the first-order splitting error that Equation (17) introduces.

In the implementation of the fractional-step procedure, a slight change in the final step, Equation (11), is made so that efficient tridiagonal solvers can be used and iteration on $\mathbf{v}^{n+1}$ is avoided. The viscous term in Equation (11) is replaced by

$$\mathbf{L}^{n+1} = \frac{2}{Re}(\nabla^2\mathbf{v}^{n+1} - \mathbf{S}^{n+1} + 2\mathbf{S}^n - \mathbf{S}^{n-1}), \tag{18}$$

where

$$\mathbf{S} = \left(-\frac{2}{r^2}\frac{\partial v}{\partial\theta}\,\mathbf{e}_r + \frac{2}{r^2}\frac{\partial u}{\partial\theta}\,\mathbf{e}_\theta\right),$$

with $\mathbf{e}_r$ and $\mathbf{e}_\theta$ being the unit vectors in the radial and circumferential directions, respectively. This treatment introduces an error, second-order accurate in time, which is consistent with the time-discretization accuracy. In flows with solid boundaries and high velocity gradients in some regions, the effect of this error is not significant because, when viscous terms are important, the second-order derivatives are the dominant parts in these terms. The terms

represented by **S** are only first-order circumferential derivatives, and therefore are small. In terms of the control of the divergence of velocity, the different treatments of **S** also only adds a term which is second-order in time to Equation (15).

3.2. Fourier spectral method

Because there is only one direction (the radial direction) which does not have a periodic boundary condition, a combined Fourier spectral approximation and finite-difference scheme are used to discretize the system of equations, Equations (9)–(14), in space. The three velocity components and the pressure can be expressed in general as functions of time and space. Let $f(r, \theta, z, \tau)$ represent any of the velocity components or the pressure and decompose $f(\,)$ as

$$f(r, \theta, z, \tau) = \sum_{l=-L/2}^{L/2-1} \sum_{k=-N/2}^{N/2-1} f_{kl}(r, \tau)\, \mathrm{e}^{ik\theta}\, \mathrm{e}^{i2\pi lz/Z}, \tag{19}$$

where $i = \sqrt{-1}$, N and L are, respectively, the number of collocation points in the circumferential and axial directions, and Z is the length of the computational domain in the axial direction.

In these formulae, the terms with $l = -L/2$ or $k = -N/2$ are present because of the fast Fourier transform, which is used extensively in the solution process and requires an even number of terms with which to work. In calculations, the coefficients of these terms are always set to zero to satisfy the conjugate symmetry of the Fourier coefficients of real variables.

3.3. Transformed equations

In the radial direction, the co-ordinate transformation,

$$r = \mathrm{e}^{\xi}, \tag{20}$$

is used to generate a finer physical mesh near the wall of the cylinder than further away from it. Thus, a uniform mesh size of $\Delta\xi$ can be specified in the computational domain because the variations of flow variables are greater near the wall.

From now on, the transformed equations and boundary conditions presented will be in the transformed system of τ, ξ, and the Fourier coefficients. The equations to solve in this system are

$$\frac{1}{\alpha}\frac{\hat{\mathbf{v}}_{kl} - \mathbf{v}^n_{kl}}{\Delta\tau} = -\frac{1}{2}(3\mathbf{N}^n_{kl} - \mathbf{N}^{n-1}_{kl}) + \frac{1}{2}\mathbf{L}^n_{kl}, \tag{21}$$

$$\left(\frac{1}{r^2}\frac{\partial^2}{\partial\xi^2} - \frac{k^2}{r^2} - \sigma^2 l^2\right)\Phi^{n+1/2}_{kl} = \frac{(\nabla\cdot\hat{\mathbf{v}})_{kl}}{\Delta\tau}, \tag{22}$$

$$\frac{\tilde{\mathbf{v}}_{kl} - \hat{\mathbf{v}}_{kl}}{\Delta\tau} = -\left(\frac{1}{r}\frac{\partial}{\partial\xi}\mathbf{e}_r + ik\mathbf{e}_\theta + i\sigma l\mathbf{e}_z\right)\Phi^{n+1/2}_{kl}, \tag{23}$$

and

$$\frac{\mathbf{v}^{n+1}_{kl} - \tilde{\mathbf{v}}}{\Delta\tau} = \frac{1}{2}\mathbf{L}^{n+1}_{kl}, \tag{24}$$

where $-L/2+1 \le l \le L/2$, $-N/2+1 \le k \le N/2-1$, and $\mathbf{e}_r$, $\mathbf{e}_\theta$, and $\mathbf{e}_z$ are the unit vectors in the radial, circumferential, and axial directions, respectively.

The calculation of the nonlinear terms in Equation (21) is the most time-consuming part in the computation. First the Fourier coefficients of velocity and vorticity need to be calculated,

then their physical values at the collocation points need to be obtained. The physical values of the nonlinear terms are then obtained at these collocation points. Finally, they are transformed to the wave space to give the Fourier coefficients of the nonlinear terms. The Poisson equation, which usually takes most of the time in totally finite-difference formulations, is reduced to a system of tridiagonal equations, as will be seen later. The operation count for solving the Poisson equation is therefore $O(MNL)$, in contrast with the operation count for the nonlinear terms, which is $O(MNL\ 1\log_2(NL))$ when the fast Fourier transform (FFT) is used. The rotational form of the convective terms is chosen because of its stability features in spectral approximations. (See Canuto *et al.* [25]). It also has an advantage over the traditional form $(\mathbf{v}\cdot\nabla\mathbf{v})$ in computational time needed. The rotational form needs a total of nine FFT operations (one inverse FFT for each of u, v, w, ω_r, ω_θ, and ω_z; one FFT for each component of the non-linear terms) per time step. The traditional form needs a total of 15 (one inverse FFT for each of the three velocity components and their nine derivatives; one FFT for each of the component of the convective terms) per time step. The utilization of the rotational form of the convective terms results in a significant reduction in computational time.

As is well-known, the computation of non-linear terms introduces aliasing errors unless special steps are taken for their removal. (See Canuto *et al.* [25]). These methods for removing aliasing errors generally require significant increases in computational effort, especially for spectral approximation in more than one direction. In the current implementation, the aliasing errors are not specifically removed. These aliasing errors are small in the flow conditions of interest here. The aliasing errors are most severe in the direct simulation of the transition process [26].

3.4. Finite-difference scheme

In this study, a half-staggered grid was used, as shown in Figure 1. All of the vector components are determined at the intersection of solid lines, whereas all of the scalars (pressure, divergence, etc.) are defined on points which are the intersections of solid and dashed lines. This grid is chosen over the fully staggered grid, where each vector component is defined at half a grid, offset in its direction from the points where scalars are defined, because the accurate calculation of the

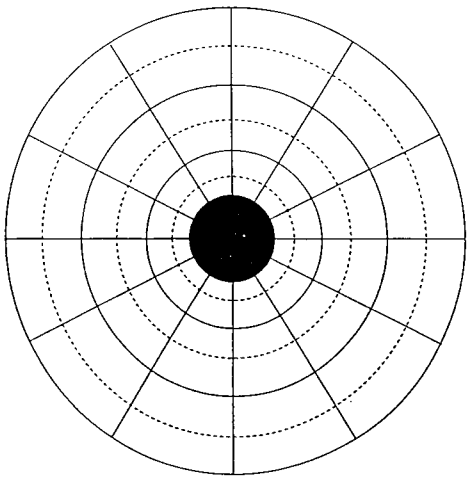

Figure 1. The half staggered grid in the (r, θ)-plane. The grid system is the same on the (r, θ)-plane for each axial collocation point. Vectors are defined at the intersections of solid lines, and scalars are defined on the intersections of solid and dashed lines.

fluid forces on the cylinder is desired, and therefore the satisfaction of no-slip boundary conditions becomes important. The half-staggered grid in combination with the viscous correction step described earlier will ensure the no-slip and no-penetration conditions are exactly satisfied. In a fully staggered grid, there will always be a slip velocity. The normal components of the vectors are defined on the wall to make the boundary condition of pressure defined on the wall and pressure defined in the flow field. The circumferential and axial components of vectors, including velocity, are thus defined at half a grid point away from the wall. Although the resulting slip velocity is small, it changes the shear stress on the wall and thus changes the magnitude and phase of the fluid forces due to shear stress. Patankar [27] has an enlightening discussion on the use of staggered grids.

It would be ideal if the pressure can also be defined on the wall so that a more accurate calculation of fluid forces due to pressure can be made. The literature shows that a straightforward implementation of the second-order centered finite-difference scheme of the pressure gradient on this grid system will result in the uncoupling of odd- and even-numbered grid points, thus producing numerical oscillations in the pressure field, which is the so-called checker-board behavior. This problem can be overcome if a compact difference scheme is used (see Lecointe and Piguet [28]). Compact difference schemes use all the grid points to determine derivatives of a variable, so the uncoupling grid is not an issue. However, since the boundary condition on pressure is on its normal derivative at the wall, defining the pressure at the boundary will result in the discarding of the source terms of the Poisson equation at the boundary. At best, these sources can only be incorporated into the solution indirectly. This, in turn, implies that the pressure correction in divergence control is not accomplished at the boundary. Thus, for complex flows with high gradients near the wall, the continuity equation is severely violated, and the numerical simulation will usually fail because of large errors in mass conservation. Therefore, the pressure on the wall is not easily defined or at the same points as the velocity is defined. A half-staggered grid thus gives the best balance between different factors of concern in the current study. Then the pressure on the wall for both the calculation of velocity and fluid forces must be found. Fortunately, the variation of pressure near solid walls is not as steep as that of velocity. Thus, an extrapolation procedure, which is based on the pressure values in the flow field and the pressure gradient on the wall, is used to obtain the wall pressure.

3.5. The pressure equation

The discrete Laplacian operator for the Poisson equation needs to be consistent with the gradient and divergence operators, which are, respectively,

$$(\nabla p)_{i,kl} = \frac{p_{i+1/2,kl} - p_{i-1/2,kl}}{r_i \Delta\xi}\,\mathbf{e}_r + j\left(\frac{k}{r_i}\,\mathbf{e}_\theta + \sigma l \mathbf{e}_z\right)\frac{p_{i+1/2,kl} + p_{i-1/2,kl}}{2}, \tag{25}$$

and

$$(\nabla \cdot \mathbf{G})_{i+1/2,kl} = \frac{1}{r_{i+1/2}}\left(\frac{A_{i+1,kl} - A_{i,kl}}{\Delta\xi} + \frac{A_{i+1,kl} + A_{i,kl}}{2}\right) + j\frac{k}{r_{i+1/2}}\frac{B_{i+1,kl} + B_{i,kl}}{2} + j\sigma l\frac{C_{i+1,kl} + C_{i,kl}}{2}, \tag{26}$$

where $\mathbf{G}$ is a vector and A, B, and C are its radial, circumferential, and axial components, respectively; $j = \sqrt{-1}$ to avoid confusion of indices. Combining Equations (25) and (26), the discrete Laplacian operator for the Poisson equation is obtained. For each pair of modes (k, l), the Poisson equation for the pressure term, Φ, is now a tridiagonal algebraic equation.

The Poisson equation for Φ and the boundary conditions (which are a combination of the

Neumann boundary conditions and periodic boundary conditions) cannot uniquely determine Φ. The solutions of the Poisson equation differ by an arbitrary constant, reflecting the lack of thermodynamic meaning of pressure in incompressible flows. In the numerical implementation, the end row of the coefficient matrix of the system of algebraic equations is reduced to all zeros by the forward sweep of the Thomas algorithm for the tridiagonal equation when both k and l are zero. The arbitrary constant is set by setting the Fourier coefficients of the mode $k = l = 0$ at the end of the forward sweep ($i = 3/2$ in the calculations since the forward sweep is from the outer boundary to the wall of the cylinder) to zero.

3.6. Outflow boundary conditions

Boundary conditions for pressure at the outer boundary are not a trivial issue in this study, as they may influence the inner flow by the incompressible nature of the fluid. Development of appropriate boundary conditions for pressure and velocity at the outer boundary, especially at outflow or mixed inflow–outflow boundaries, have been discussed by many researchers, such as Sani and Gresho [29] and Mittal and Balachandar [30]. However, because of the complexity of the problem and the large variation of flow conditions, no widely applicable formulation of boundary conditions at numerically truncated boundaries (open boundaries) is currently available.

The effect of the pressure boundary condition needs to be minimized, especially its 2D effect, so that the 3D instabilities are not numerically suppressed. Ideally, pressure should be determined by the flow. The boundary conditions should reflect this nature. Thus, the radial derivative of pressure, derived from the radial component of the momentum equations, is used as the boundary condition for steady approach flows.

The outflow boundary conditions for velocity should be such that the boundary condition should not interfere with the outflow passage of vortices and also should not affect the global properties of the flow, such as drag, lift, and vortex shedding. Thus, the following conditions are used at the outflow boundary

$$\frac{\partial(\omega_r)_{kl}}{\partial r} = \frac{\partial(\omega_\theta)_{kl}}{\partial r} = \frac{\partial(\omega_z)_{kl}}{\partial r} = 0, \tag{27}$$

and

$$\frac{\partial^2 u_{kl}}{\partial r^2} = \frac{\partial u_{kl}}{\partial r} = 0, \tag{28}$$

where ω_r, ω_θ, ω_z represent the three vorticity components, as determined from the computed velocities, and kl represents the kl mode in the spectral representation. Allowing the vorticity to pass through the boundary undisturbed by the boundary is the most natural boundary condition that can be applied.

4. CALCULATION OF THE FORCE COEFFICIENTS

The fluid forces on the cylinder can be decomposed into two parts: the contributions due to pressure and shear stress. Over the entire cylinder length, the force coefficients are

$$C_D = -\frac{1}{Z}\int_0^z \int_0^{2\pi} \left(p\cos\theta + \frac{2}{Re}\,\omega_z \sin\theta \right)_{r=1} \mathrm{d}\theta\, \mathrm{d}z \tag{29}$$

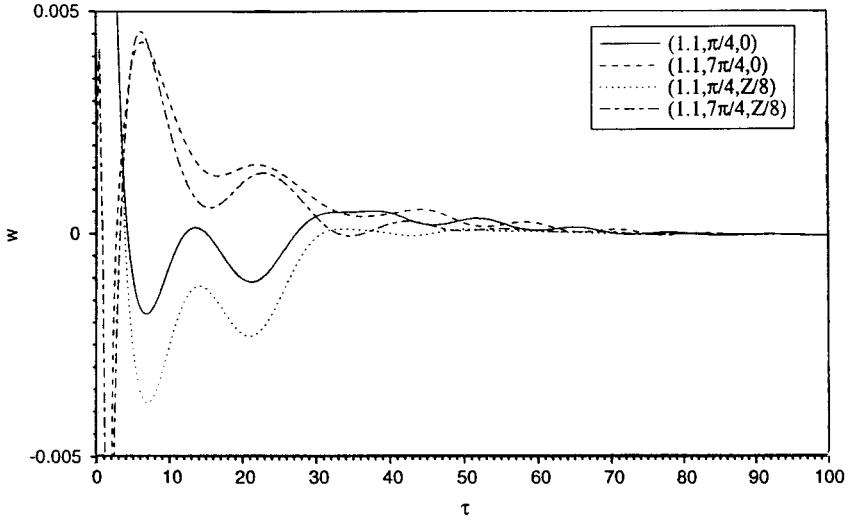

Figure 2. Axial velocity at four different locations for $Re = 100$. The co-ordinates shown are (r, θ, z).

and

$$C_L = -\frac{1}{Z}\int_0^z \int_0^{2\pi} \left(p \sin\theta - \frac{2}{Re}\omega_z \cos\theta \right)_{r=1} \mathrm{d}\theta \, \mathrm{d}z, \tag{30}$$

where C_D and C_L are the drag and lift coefficients, respectively, Z is the cylinder length, and p and ω_z are evaluated on the cylinder surface. Since both pressure and vorticity are z-dependent, sectional values of both drag and lift can be determined by suppressing the z-direction integration in Equations (29) and (30) and using local (at a particular value of z) distributions of p and ω.

5. NUMERICAL RESULTS

5.1. $Re = 100$

At $Re = 100$, the physical flow is 2D with an unsteady wake. A 3D simulation was performed and the velocity from the start of the calculation $\tau = 0$ to $\tau = 5$ was perturbed. The grid had 128 radial points and 128 and 32 Fourier collocation points in the circumferential and axial directions, respectively. The outer boundary was at 21.3 cylinder diameters, the cylinder length was set at $Z = 11$ and the time step was 0.01. The adequacy of these values will be discussed later. Figure 2 shows the behavior of the axial velocity with time for four different (r, θ) positions. The damping of the perturbation with time is quite clear from the plots in Figure 2, i.e., the resulting calculated flow is clearly 2D. Figure 3 shows the contours in the plane $z = 0$ at $\tau = 100$. There is essentially no distortion of the vortices as they pass through the outflow boundary which indicates the appropriateness of the outflow boundary conditions used. Figure 4 shows that the ω_z isolines are 2D at $\tau = 100$, i.e., the effects of the axial perturbations have been completely damped. These isolines are plotted in the computational plane rather than the physical plane to show the radial variation of vorticity more clearly, especially in the wall region. The line $\xi = 0$ represents the cylinder wall and $\xi = 3.75$ represents

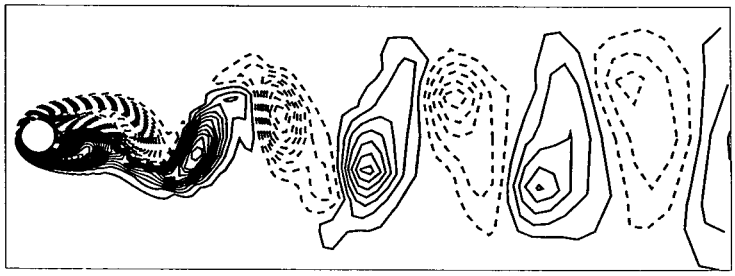

Figure 3. Contours of ω_z at $\tau = 100$ and $z = 0$ with $Re = 100$.

the outflow boundary. The fact that the isovorticity lines are parallel to the cylinder wall and perpendicular to the direction of flow indicates that the flow in the wake is 2D and that the perturbations have been damped. The drag and lift coefficients, shown in Figure 5, agree quite well with the experimental data. The drag coefficient has an average value of 1.32, which compares well with the experimental value of 1.3. The lift coefficient has a peak of 0.32. The computed Strouhal frequency is 0.154, which is within the experimental range of 0.15–0.16 at $Re = 100$.

5.2. $Re = 200$

The physical flow at $Re = 200$ has a 3D viscous wake. As stated earlier, the transition from a 2D to a 3D wake occurs at a Reynolds number of about 170. Thus, the test of the 3D capability of the numerical method is the growth of the disturbances at $Re = 200$.

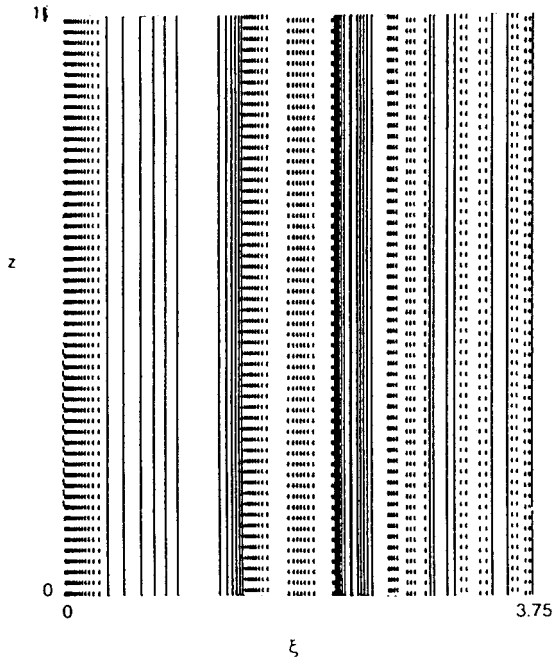

Figure 4. Isolines of ω_z on the computational plane at $\tau = 100$ and $\theta = 0$ with $Re = 100$.

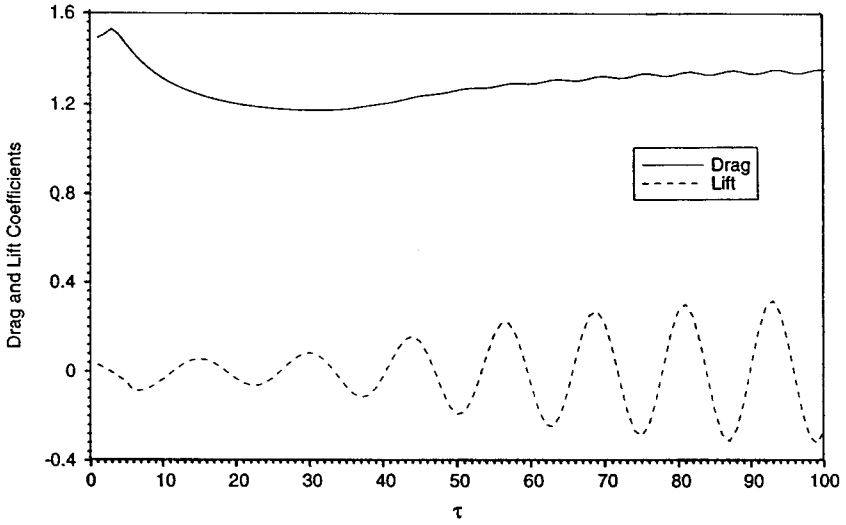

Figure 5. Drag and lift coefficients for steady approach flow at $Re = 100$.

First, the $Re = 200$ case was computed as a 2D flow to discuss convergence and stability. Table I shows the comparison of three different mesh sizes; with the mesh of 160×128 yielding the best comparison with the experimental data. Table I also shows a time-step comparison for the 160×128 mesh, which indicates that a time step of 0.01 is adequate for a stable converged solution. (The calculation did become unstable for a time step of 0.02). Each of the calculations shown in Table I was carried to a dimensionless time of $\tau = 100$. To further illustrate convergence, the maximum divergence of velocity (at $i = 1$) is presented in Figure 6 which shows that the 160×128 mesh has produced a constant and satisfactory value of the divergence. Since the Cray C90, with its 64-bit floating-point calculations, was used for these calculations, the effect of round-off error was deemed to be insignificant for both 2D and 3D flows. The physical flow at $Re = 200$ has an unsteady wake formed by shed vortices. The vortex-shedding phenomenon was allowed to happen naturally, so the occasion of a shed vortex did not occur at precisely the same time for each mesh system. Therefore, global quantities, such as drag and lift, were used as the criteria for convergence as opposed to the actual variables being computed.

The effect of the outer boundary on the flow was examined by considering two different outer boundary lengths in the transformed co-ordinate system. These two lengths led to outer boundary lengths of $r_\infty = 99.48$ and 198.34 in the physical plane. There was no discernible

Table I. Averaged drag coefficient (C_D), peak lift coefficient (C_L), and Strouhal frequency (S) for steady approach flow at $Re = 200$ from two-dimensional calculations with $\Delta\tau = 0.005$ and $r_\infty = 99.48$

M	N	$\Delta\tau$	$C_{D,C}$	$C_{D,E}$	$C_{L,C}$	S_C	S_E
160	128	0.005	1.32	1.22–1.3	0.68	0.198	0.178–0.196
80	64	0.005	1.34		0.69	0.197	
40	32	0.005	<1.1		0.55	0.165	
16	128	0.01	1.31		0.68	0.197	

Subscripts C and E refer to calculated and experimental values respectively.

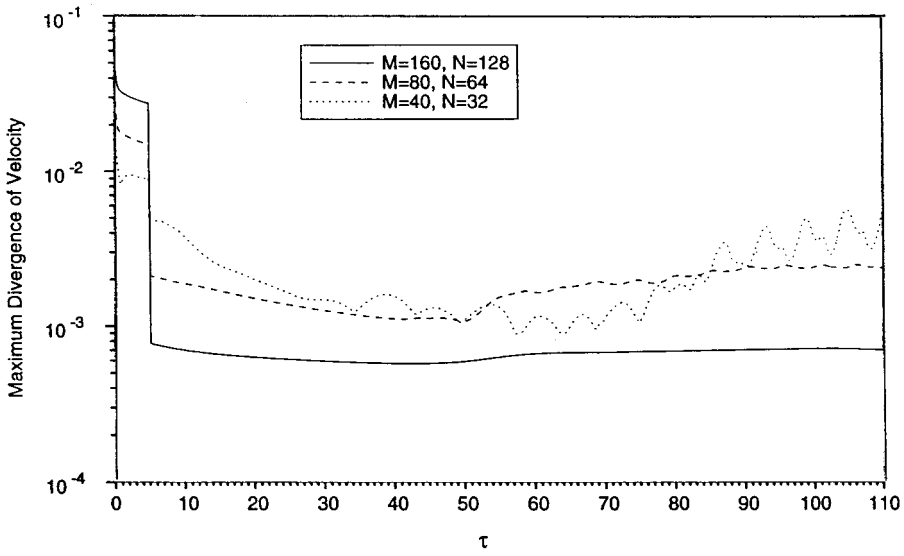

Figure 6. Maximum divergence of velocity at $i = 1$ for steady approach flow at $Re = 200$. Divergence is defined on $i + 1/2$. In the two-dimensional calculations, $r_\infty = 99.48$ and $\Delta\tau = 0.005$.

difference in the drag and lift plots for the two different outer boundaries for $\Delta\xi = 0.02875$ and $N = 128$ and a time step of 0.005. Thus, one can conclude that an outer boundary of $r_\infty = 99.48$ is sufficiently large.

In the physical flow for $Re = 200$, there are spanwise (axial) periodic structures which have developed. Thus, an axial length of the cylinder, that is sufficiently long so that the periodic boundary condition in the axial direction can be satisfied, must be chosen. Obviously, some error will be introduced since the assumed wavelength will not be an integer multiple of the natural wavelength. Selecting the axial computational domain long enough will allow the simulation to amplify those modes that are closest to the natural wavelengths. Careful tests have revealed that an axial length value of $Z = 15$ is sufficient for the axial modes to be captured accurately.

The 3D vorticity results for $Re = 200$ are shown in Plates 1–3 for a mesh of 160 radial divisions and 128 and 48 Fourier collocation points in the circumferential and axial directions, respectively. The time step was 0.002, the outer boundary was 99.48 radii and the axial length was 15. The calculations took 15 s per time step on the Cray C90 at the Pittsburgh Supercomputer Center. The calculation speed was in excess of 400 MFlops. In Plates 1–3, the vorticity value being shown is $\omega_z = \pm 0.5$ at two different times, $\tau = 102.5$ and 105. Plate 1 shows the clear 3D behavior of the vortex sheet being shed from the cylinder near side at $\tau = 102.5$ while Plate 2 shows the same behavior at $\tau = 105$. Plate 3 shows the backside view of the situation depicted in Plate 2. The vortex sheets on the front side of the cylinder are 2D as expected and, after separation, a slight spanwise variation of the vortex sheet has developed. The three-dimensionality continues after the vortices have been shed. Vortices which are two shedding-cycles old, shown at the right in these figures, have well developed 3D variations along their isosurfaces. These variations show that the spanwise wavelength is about half the

length of the spanwise computational domain, i.e., the wavelength is 3.75 diameters. This agrees reasonably well with the experimental observation of 3 to 3.2 diameters [7,10]. An interesting observation is that the shedding of vortices has a slight difference in time along the span, as shown in Plate 2. One result of this difference is the phase difference in the forces at different sections of the cylinder.

One of the most influencing factors on the difference of predicted wavelength and experimental observations is the length of the spanwise computational domain (Z), chosen because a forced periodicity is used in the spanwise direction. If a very large Z is used, the difference between calculation and experiment will be much smaller. However, this is not feasible computationally because many more spanwise modes are necessary to represent the dynamics of the 3D flow accurately. Later it will be shown that, although the primary 3D structures have a wavelength of 3.75 diameters, many modes with smaller wavelengths are at relatively the same strength compared with each other and are not very small in strength when compared with the primary spanwise structures. This implies that, if a value of Z is used that is about twice the physical wavelength, four or five modes in the spanwise direction may be enough to simulate the primary 3D structures. However, to get a more accurate view of the impact of three-dimensionality, many more modes (such as the 24 modes used) are necessary. The 3D mixing and the tilting and stretching of vortices, which are distinct features distinguishing 3D simulations from 2D simulations, can only then be simulated approximately. These factors make it extremely difficult to predict accurately both spanwise wavelengths and the dynamics of 3D flow. It is believed that the errors associated with the inaccurate estimation of spanwise wavelength are of no significance because they mainly imply a numerical scaling of the 3D behavior in the wake, but the physics of the flow should remain correct. This effect is much weaker than the mixing and vortex tilting and stretching. It is highly advisable, though, to be very cautious in estimating for different flow situations what the minimum length of the spanwise computational domain can be without seriously affecting the solution.

Plates 4 and 5 show the isosurfaces of the streamwise vortices, ω_x, at $\tau = 102.5$ and 1.05. The red isosurfaces have a ω_x value of 0.1 and the blue ones have a ω_x value of -0.1. Again it is seen that three-dimensionality is not present at the front part of the cylinder. At the recirculation region behind the cylinder, streamwise vortices form several periodic and interlacing structures. When the flow develops while flowing downstream, more and more variations develop in the structures of streamwise vortices. Eventually, the 3D mixing is very strong everywhere in the wake as the interlacing isosurfaces fill the whole wake. Plate 6 shows the contour lines for streamwise vorticity at three radial distances away from the center of the cylinder, $r = 1.3$, 3, and 10. The locations of the spanwise structures correspond to the locations of the axial vortices in the wake. These structures develop while the shed vortices are being convected downstream.

Figures 7–10 show the spanwise power spectrum of velocity at three locations in the centerline of the wake, i.e., $r = 1.5$, 10, and 20 with $\theta = 0$, and two other locations in the region of attached vortices, i.e., $r = 1.5$ with $\theta = \pi/4$ and $7\pi/4$. From Figures 7 and 8, it is seen that the spanwise wavelength varies very little with cross stream locations. In contrast, Figures 7, 9 and 10 show that the spanwise wavelength increases with streamwise locations, from 2.5 diameters near the cylinder ($r = 2.5$) to 3.2 diameters at five diameters away from the center of the cylinder. It seems that the same wavelength stabilizes at 3.2 diameters after $r = 10$, as Figure 10 shows the same wavelength. These differences are more obvious in the spectra for w than for u and v because the latter are controlled not only by three-dimensionality, but also by the primary 2D structures. As a result, the behaviors of the wavelengths for u and v are more complex than that of w. These spectra all show large values at a wavelength of 15, which is the size of the spanwise computational domain. This feature shows that a large part of the

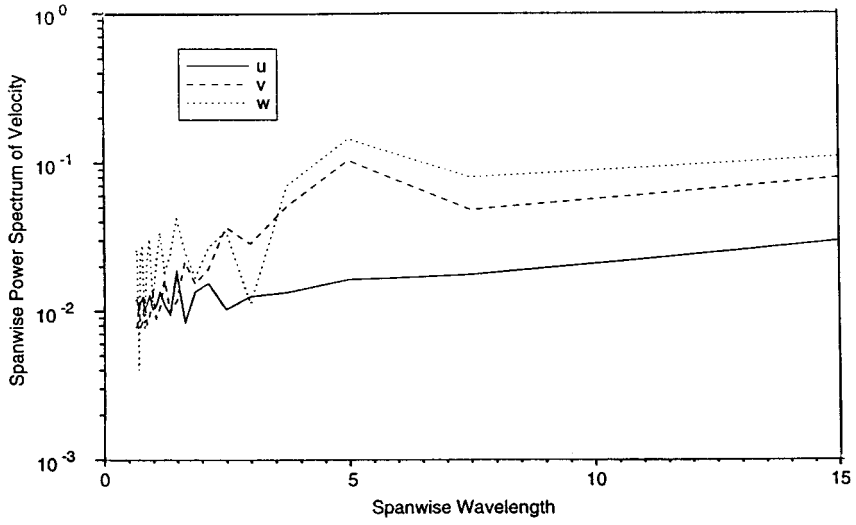

Figure 7. Spanwise power spectra of velocity at $r = 1.5$ and $\theta = 0$ for $Re = 200$ and $\tau = 105$.

spectrum for each velocity component is the part which is invariant with z (mode $l = 0$). For u and v, it is obvious that these invariant parts reflect the primary flow. For w, the existence of a strong $l = 0$ mode is because, at a particular time and a particular (r, θ) location, there is a nonzero average axial velocity. This average may switch signs and change values as vortices pass by, or for the points close to the cylinder, as the vortex shedding process makes the size of attached vortices change.

The 3D simulation corrects the trend to overpredict drag coeffficients and Strouhal frequency in 2D simulations. Figure 11 shows the drag and lift coefficients from both 2D and 3D calculations. Both the average drag and the maximum lift coefficients from the 3D simulations are smaller than the corresponding values from 2D simulations with the same time

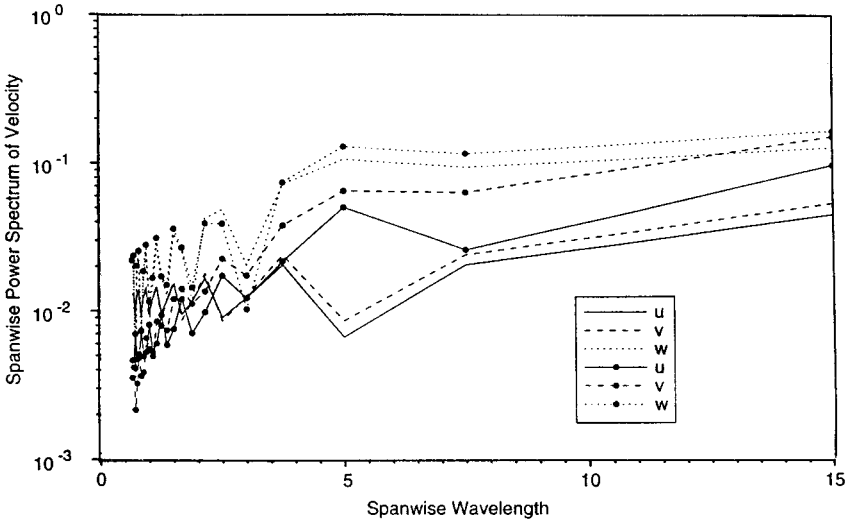

Figure 8. Spanwise power spectra of velocity at $r = 1.5$ and $\theta = \pi/4$ (solid line) and $7\pi/4$ (solid line with dots) for $Re = 200$ and $\tau = 105$.

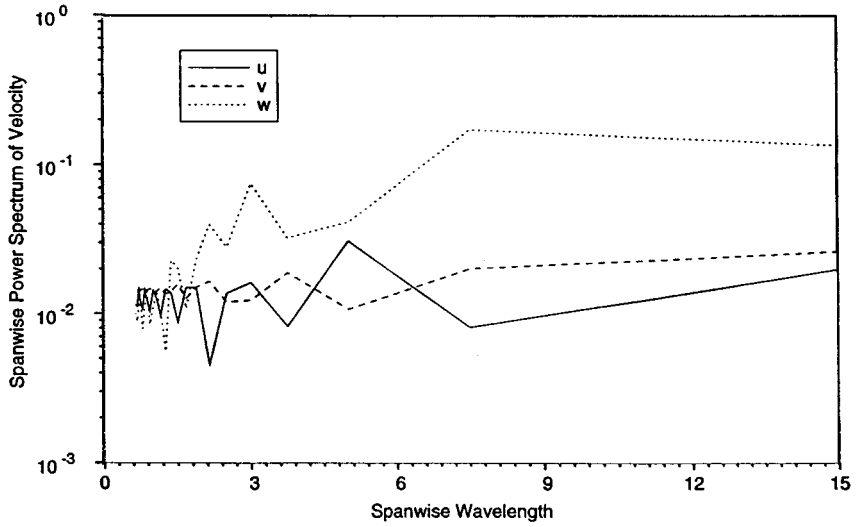

Figure 9. Spanwise power spectra of velocity at $r = 10$ and $\theta = 0$ for $Re = 200$ and $\tau = 105$.

step and spatial resolution in the (r, θ) plane. The average C_D is 1.32 with 2D simulation and 1.28 with 3D simulation, compared with experimental values ranging from 1.3 to 1.22 [31–32]. The maximum lift coefficient is 0.68 with 2D simulation and 0.61 from 3D simulation. The difference comes from the phase difference and thus the canceling of sectional fluid forces in 3D simulations, which is a physical reality and is absent in 2D simulations. Although the vortex strength and sectional fluid forces are of about the same magnitude at different spanwise locations, the 3D mixing of the wake makes the averages smaller in magnitude. In Figure 12, it is seen that the sectional drag coefficients can have magnitudes larger than the average drag coefficient. There are phase differences between the sectional drag coefficients, which is the reason for the smaller average. Similar situations are present in the sectional lift

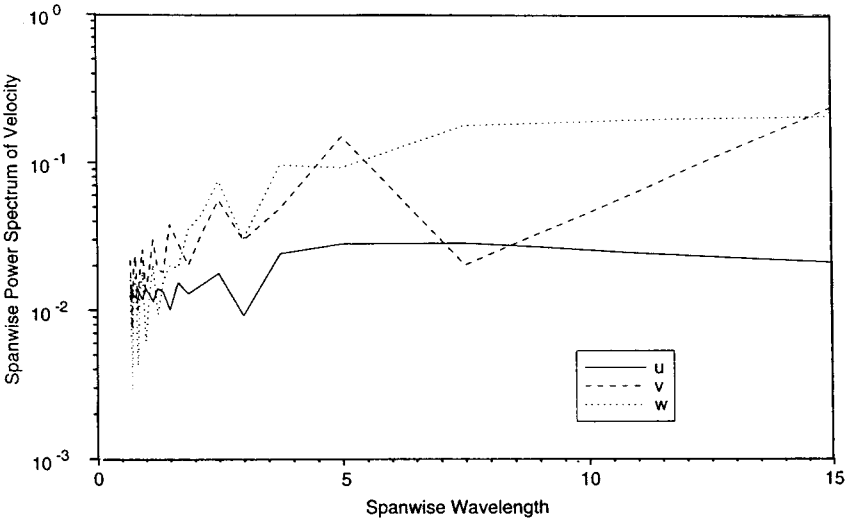

Figure 10. Spanwise power spectra of velocity at $r = 20$ and $\theta = 0$ for $Re = 200$ and $\tau = 105$.

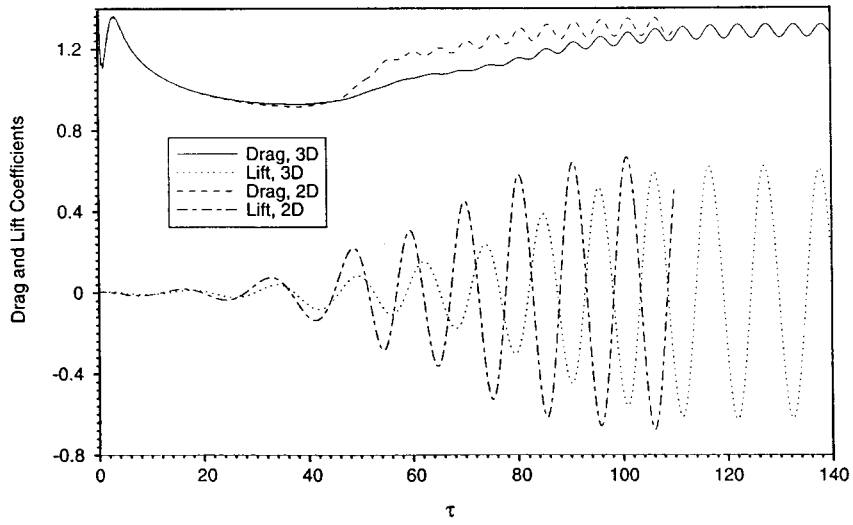

Figure 11. Comparison of drag and lift coefficients obtained by two- and three-dimensional simulations with same time step and spatial resolution in the (r, θ)-planes for $Re = 200$.

coefficients, shown in Figure 13. This phase difference corresponds to the phase differences in the shedding of vortices along the span, as mentioned earlier.

The Strouhal frequency is also smaller in the 3D simulation than the 2D simulation. From the 3D simulation, the Strouhal frequency is 0.190, and from the 2D simulation, it is 0.199. The 3D simulation gives better agreement with experimental values of 0.178–0.196 [4].

The lower value of the Strouhal frequency in the 3D simulation is due to the z-direction transfer of momentum in the wake. The rate of growth of the wake vortices is apparently inhibited by the development of the axial component of velocity which is not present in the 2D simulations. It is conjectured that the intensity of the wake vortices is diminished in 3D due to the axial momentum transfer, leading to a slight decrease in shedding frequency as compared with the 2D case.

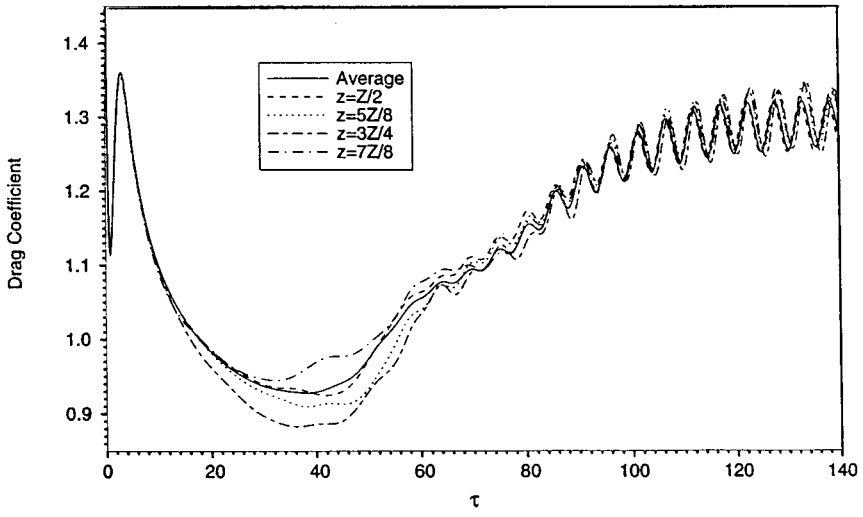

Figure 12. Average and sectional drag coefficients for $Re = 200$ at $z = Z/2$, $5Z/8$, $3Z/4$, and $7Z/8$.

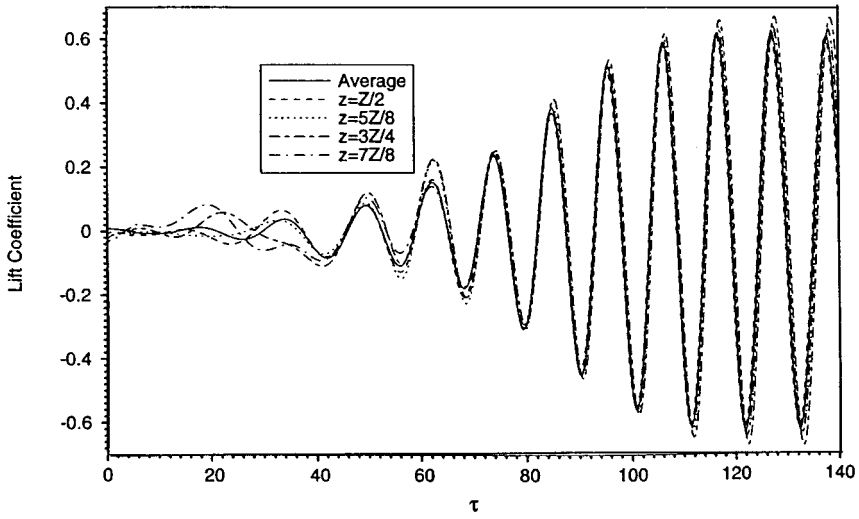

Figure 13. Average and sectional lift coefficients for $Re = 200$ at $z = Z/2$, $5Z/8$, $3Z/4$, and $7Z/8$.

6. CONCLUSIONS

A 3D primitive-variables solution of the incompressible Navier–Stokes equations was performed using a fractional-step method to advance time. The physical problem was flow past a circular cylinder at $Re = 100$ and 200. The $Re = 100$ case is a 2D flow and the computed results agreed quite well with the experimental values.

At a Reynolds number of 200, the wake shows distinct 3D structures with spanwise wavelength of 3.75 diameters of the cylinder. The spanwise wavelength increases with downstream locations and stabilizes after about ten diameters away from the cylinder. Three-dimensionality is shown to not only increase the mixing in the wake, but also tilt and stretch the vortices in the Karman vortex sheet. The 3D simulation produces smaller global quantities (with better agreement with experimental values), such as drag and lift coefficients and Strouhal frequencies, than the corresponding 2D simulation with the same spatial and temporal resolution. The difference is attributed to the phase difference of flows in different spanwise locations caused by three-dimensionality and the 3D mixing, which are both absent in the 2D simulation. It is concluded that three-dimensionality is an important and inherent part of the steady approach flow with higher than moderate Reynolds number and that 3D simulations are necessary for reliable modeling of these flows.

However, 2D simulations are much less expensive than 3D simulations; so, if a cautious estimate is made on the effect of the lack of the 3D features, one can still use 2D simulations to obtain a qualitative understanding of the flow.

ACKNOWLEDGMENTS

The authors are grateful to NSF for grant ID INT924844 and to the Pittsburgh Supercomputing Center for grant CBT91004P used in support of this project. They are also grateful to Professor Lixian Zhuang (of the University of Science and Technology of China) who spent his sabbatical with them at the University of Houston during the early part of this study.

REFERENCES

1. G.E. Karniadakis, M. Israeli and S.A. Orszag, 'High-order splitting methods for the incompressible Navier–Stokes equations', *J. Comp. Phys.*, **59**, 308–323 (1991).
2. J. Kim and P. Moin, 'Application of a fractional step method to incompressible Navier–Stokes equations', *J. Comp. Phys.*, **59**, 308–323 (1985).
3. M.S. Bloor, 'The transition to turbulence in the wake of a circular cylinder', *J. Fluid Mech.*, **19**, 290–304 (1964).
4. A. Roshko, 'On the development of turbulent wakes from vortex streets', *NACA Rep.* **1191**, 1–23 (1954).
5. F.R. Hama, 'Three-dimensional vortex patterns behind a circular cylinder', *J. Aerosp. Sci.*, **24**, 156–157 (1957).
6. J.H. Gerrard, 'The wakes of cylindrical bluff bodies at low Reynolds number', *Philos. Trans. R. Soc. Lond. A*, **288**, 351–382 (1978).
7. C.H.K. Williamson, 'The existence of two stages in the transition to three-dimensionality of a cylinder wake', *Phys. Fluids*, **31**, 3165–3168 (1988).
8. B.R. Noack and H. Eckelmann, 'A global stability analysis of the steady and periodic cylinder wake', *J. Fluid Mech.*, **270**, 297–330 (1994).
9. M. König, B.R. Noack and H. Eckelmann, 'Discrete shedding modes in the von Karman vortex street', *Phys. Fluids A*, **5**, 1846–1848 (1993).
10. H. Mansy, P.M. Yang and D.R. Williams, 'Quantitative measurements of three-dimensional structures in the wake of a circular cylinder', *J. Fluid Mech.*, **270**, 277–296 (1994).
11. B. Bays-Muchmore and A. Ahmed, 'On streamwise vortices in turbulent wakes of cylinders', *Phys. Fluids A*, **164**, 387–392 (1993).
12. C.H.K. Williamson, 'Oblique and parallel modes of vortex shedding in the wake of a circular cylinder at low Reynolds numbers', *J. Fluid Mech.*, **206**, 579–627 (1989).
13. C.G. Lewis and M. Gharib, 'An exploration of wake three-dimensionalities caused by a local discontinuity in cylinder diameter', *Phys. Fluids A*, **4**, 104–117 (1992).
14. C.H.K. Williamson, 'The natural and forced formation of spot-like vortex dislocations in the transition of a wake', *J. Fluid Mech.*, **243**, 393–441 (1992).
15. P.M. Yang, H. Mansy and D.R. Williams, 'Oblique and parallel wave interaction in the near wake of a circular cylinder', *Phys. Fluids A*, **5**, 1657–1660 (1993).
16. M. Hammache and M. Gharib, 'A novel method to promote parallel vortex shedding in the wake of a circular cylinder', *Phys. Fluids A*, **1**, 1611–1614 (1989).
17. P.M. Gresho, R. Chan, C. Upson and R. Lee, 'A modified finite element method for solving the time-dependent, incompressible Navier–Stokes equations, Part 2. Applications', *Int. j. numer. methods fluids*, **4**, 619–640 (1984).
18. M. Braza, P. Chassaing and H. Ha Minh, 'Numerical study and physical analysis of the pressure and velocity fields in the near wake of a circular cylinder', *J. Fluid Mech.*, **165**, 79–130 (1986).
19. M. Braza, P. Chassaing and H. Ha Minh, 'Prediction of large-scale transition features in the wake of a circular cylinder', *Phys. Fluids A*, **2**, 1461–1471 (1990).
20. G.E. Karniadakis and G.S. Triantafyllou, 'Frequency selection and asymptotic states in laminar wakes', *J. Fluid Mech.*, **199**, 441–469 (1989).
21. T. Tamura, I. Ohta and K. Kuwahara, 'On the reliability of two-dimensional simulation for unsteady flows around a cylinder-type structure', *J. Wind Eng. Ind. Aerodyn.*, **35**, 275–298 (1990).
22. X. Wang and C. Dalton, 'Numerical solutions for impulsively started and decelerated viscous flow past a circular cylinder', *Int. j. numer. methods fluids*, **12**, 383–400 (1991).
23. G.E. Karniadakis and G.S. Triantafyllou, 'Three-dimensional dynamics and transition to turbulence in the wake of bluff objects', *J. Fluid Mech.*, **238**, 1–30 (1992).
24. M.O.L. Hansen, J.N. Sorensen and V.A. Barker, 'A numerical investigation of 3D flow past an infinite cylinder', *AFM 92-03, ISSN 0590-8809*, Department of Fluid Mechanics, Technical University of Denmark, 1992.
25. C. Canuto, M.Y. Hassaini, A. Quarteroni and T.A. Zang, *Spectral Methods in Fluid Dynamics*, Springer, Berlin, 1988.
26. S. Krist and T.A. Zang, 'Numerical simulation of channel flow transition: resolution requirements and the structure of the hairpin vortex', *NASA TP-2667*, 1987.
27. S.V. Patankar, *Numerical Heat Transfer and Fluid Flow*, McGraw-Hill, New York, 1980.
28. Y. Lecointe and J. Piquet, 'Compact finite difference methods for solving incompressible Navier–Stokes equations around oscillating bodies', Von Karman Institute for Fluid Dynamics Lecture Series 1985–04, 1985.
29. R.L. Sani and P.M. Gresho, 'Resume and remarks on the open boundary condition minisymposium', *Int. j. numer. methods fluids*, **18**, 983–1008 (1994).
30. R. Mittal and S. Balachandar, 'Study of flow over an elliptic cylinder using a direct numerical simulation', FED-vol. 203, *Turbulence in Complex Flows*, ASME, New York, 1994.
31. H. Schlichting, *Boundary Layer Theory*, McGraw-Hill, New York, 1979.
32. J. Fang, 'Numerical Simulation of Unsteady Incompressible Flow past a Circular Cylinder', *MS Thesis*, University of Alabama, Huntsville, AL, 1987.

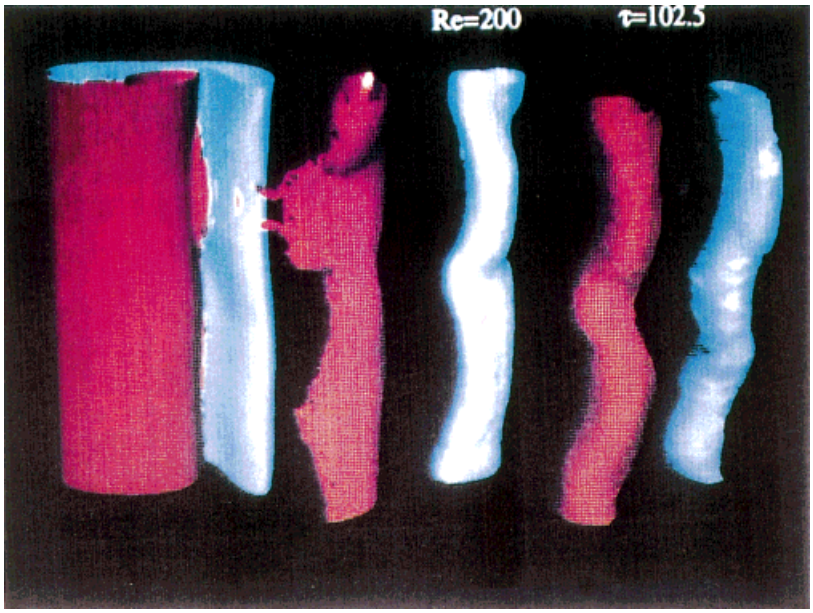

Plate 1. Isosurfaces for axial vorticity at $Re = 200$ and $\tau = 102.5$. The red surfaces are for $\omega_z = 0.5$ and the light blue surfaces are for $\omega_z = -0.5$.

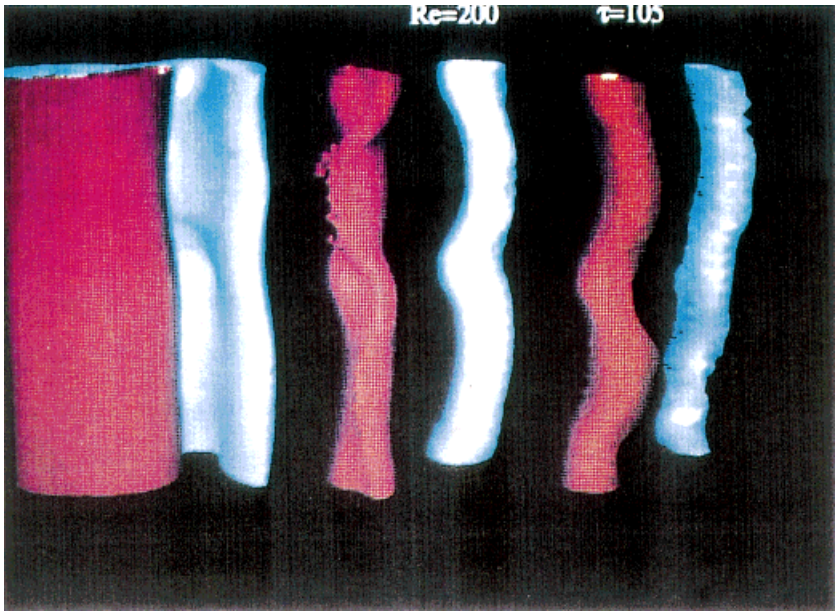

Plate 2. Isosurfaces for axial vorticity at $Re = 200$ and $\tau = 105$. The red surfaces are for $\omega_z = 0.5$ and the light blue surfaces are for $\omega_z = -0.5$.

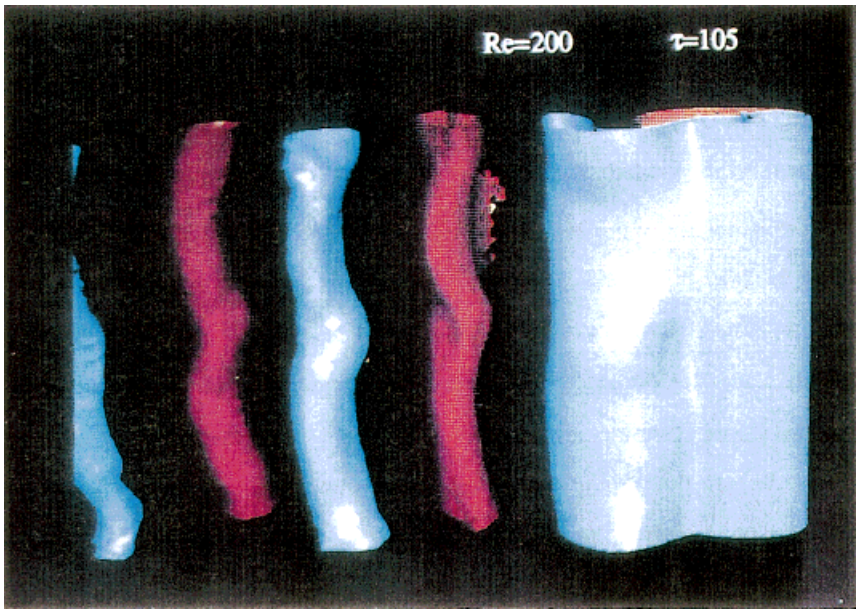

Plate 3. A view from the back of the isosurfaces in Plate 2. The direction of the freestream flow is from right to left in this figure.

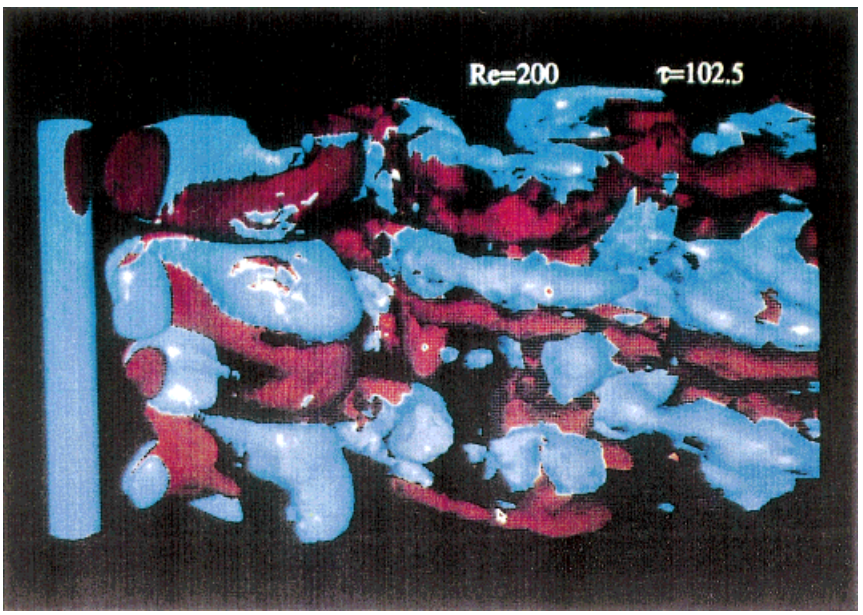

Plate 4. Isosurfaces for streamwise vorticity at $Re = 200$ and $\tau = 102.5$. The red surfaces are $\omega_x = 0.1$ and the light blue surfaces are for $\omega_x = -0.1$.

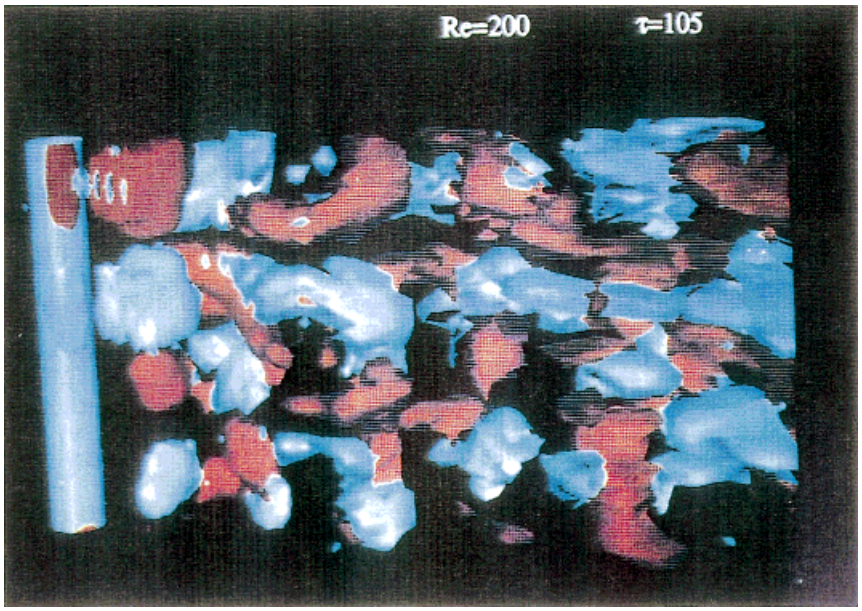

Plate 5. Isosurfaces for streamwise vorticity at $Re = 200$ and $\tau = 105$. The red surfaces are for $\omega_x = 0.1$ and the light blue surfaces are for $\omega_x = -0.1$.

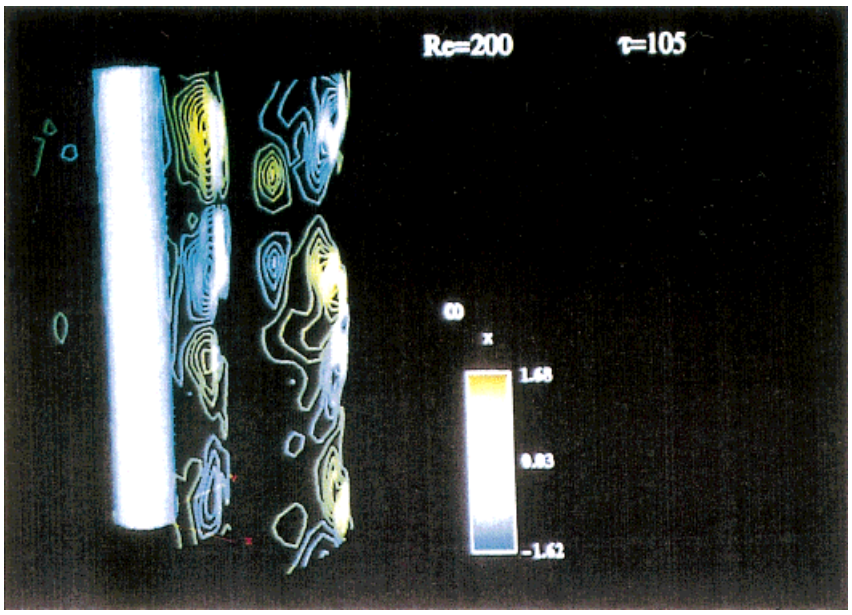

Plate 6. Contour lines for streamwise vorticity at $r = 15$, 3, and 10; $\tau = 105$; and $Re = 200$.